



## Methodology for multidimensional approximation of current velocity fields around offshore aquaculture installations



Alexander Knysh <sup>a</sup>, Andrew Drach <sup>b</sup>, David Fredriksson <sup>c</sup>, Tobias Dewhurst <sup>d</sup>, Igor Tsukrov <sup>a,\*</sup>

<sup>a</sup> University of New Hampshire, Durham, NH 03861, USA

<sup>b</sup> The University of Texas at Austin, Austin, TX 78712, USA

<sup>c</sup> United States Naval Academy, MD 21402, USA

<sup>d</sup> Kelson Marine Co., Scarborough, Maine 04074, USA

### ARTICLE INFO

**Keywords:**

Large-scale installations  
Finite element analysis  
Field measurements  
Radial basis function

### ABSTRACT

Consistent growth of the marine aquaculture industry over the past decades calls for potential deployments of large-scale aquaculture structures to produce finfish, shellfish and macroalgae in varying inshore and offshore environments. Numerical simulations for engineering design applications become more challenging with increase of scale since current velocity fields are no longer uniform, complicating accurate hydrodynamic load calculations. Horizontal and vertical velocity profiles in this case are spatially (depth and particular location within the deployment site) and temporary (date and time) dependent. Thus, proper representation of the current velocity field in numerical models becomes crucial for accurate predictions of structural performance of aquaculture installations. In this paper, an advanced multidimensional approximation method based on discrete current velocity data is formulated. The approach implies presenting the continuous current velocity function as a superposition of weighted radial basis functions extended by a linear polynomial. To address overfitting issues, the thin plate regularization is applied in the method. The approximation is then constrained in order to fit the velocity values on the domain boundaries. The method is implemented in finite element software *Hydro-FE* and its performance is compared to other approximation methods on the example of a kelp grow line deployed at the Wood Island research site, Maine, USA. It was found that the difference between regular (mean or linearly interpolated) velocity profiles and the velocity profiles approximated with the radial basis function method can reach up to 34–38 % in terms of grow line mooring tensions, and 6–18% in terms of grow line displacement.

### 1. Introduction

Aquaculture is one of the fastest growing industries and the fastest growing food sectors in the world due to increasing consumer demand in seafood, kelp and other aquaculture products (Gentry et al., 2017). To satisfy this demand, sustainable production needs to expand to inshore and offshore sites around the world that can be safely exploit/maintained from ecological and economical points of view (Fairbanks, 2016). Large-scale aquaculture deployments such as fish farms with multiple net pens, shellfish or kelp farm structures have garnered considerable attention from researchers in this context (Asche et al., 2018).

As economics of scale show profitability, adequate numerical estimate of structural performance becomes a crucial factor for successful deployment, especially in high tidal currents and potential storm events. Thus, numerous studies have been conducted providing numerical

predictions based on the appropriate field data sets. For instance, numerical modeling of the Broad Cove fish farm located in Maine, USA, was performed in finite element software *Aqua-FE* using current velocity measured by several current meters kept about 4 m below the water surface (Fredriksson et al., 2007). Similar investigations have also been conducted in Europe, where response of a large circular sea cages near the Faroe Islands was modeled in *FhSim* software developed by SINTEF Fisheries and Aquaculture, Norway (Klebert et al., 2015; Wintherig-Rasmussen et al., 2016). Volume change of one of the cages as well as forces applied on it were estimated through computational fluid dynamics analysis with current profiles recorded by acoustic doppler current profiler (ADCP) placed outside and inside of the cage. Another example is modeling of typical mussel longline system with the backbone that supports long V-shaped mussel collector lines. The behavior of the longline located near Belgian North Sea was simulated

\* Corresponding author.

E-mail address: [igor.tsukrov@unh.edu](mailto:igor.tsukrov@unh.edu) (I. Tsukrov).

with lumped-mass open-source code *MoorDyn* and compared with the commercially available *OrcaFlex* software (Pribadi et al., 2019). Currents were implemented as a uniform velocity field over the whole simulation domain. Numerical studies performed with other specialized software, such as *DUT-FlexSim* (Zhao et al., 2015; Bi et al., 2020), *SimuTrawl* (Nguyen and Winger, 2016; Thierry et al., 2019), etc., also assumed uniform velocity profiles.

While most of the existing numerical studies assume that incident horizontal and vertical velocity profiles are the same within the entire simulation domain, this is not necessarily true for most of the large-scale applications. For this reason, some ocean engineering software products implement advanced options to input velocity fields. *OrcaFlex* introduces vertical and horizontal current variations given as a magnitude with dimensionless multiplicative factor, external function that depends on spatial/time variables or interpolated data set. The user-defined data set can be interpolated with one of three methods: linear, cubic spline, cubic Bessel (<https://www.orcina.com/webhelp/OrcaFlex/Content/html/Environment,Currentdata.htm>). *ProteusDS* allows user to initialize uniform and linear shear current profiles, power law current profile commonly used in tidal channels, custom current profile that depends on time and depth only, and three-dimensional spatially varying current profile where intermediate velocity values are obtained with three-dimensional interpolation scheme (<http://documentation.dsaocean.com/tutorials/Tutorials/PDS-AAV.html>). In terms of the current velocity field accuracy, these and other software packages are limited to interpolation of user-defined current velocity data. Even though it is suitable for some applications, single- and multidimensional interpolations can fail to produce adequate interpolant due to overfitting (Smith et al., 1998).

In this paper an advanced approach to compose a smooth and accurate multidimensional approximation of the current velocity field is proposed, where the velocity function is taken as a superposition of weighted radial basis function extended by linear polynomial. The method is described in details in Section 2. Current data acquisition for the approximation method are discussed in Section 3. The section also describes acquisition of the actual current velocity field data on the example of acoustic wave and current profilers at the University of New England (UNE) Wood Island research site, Maine, USA. Section 4 is dedicated to simulations of a *Saccharia latissima* kelp farm deployed at the site with the finite element software *Hydro-FE*. The simulations are performed for the method proposed in this paper as well as for other current approximation techniques. Results are then discussed and compared in terms of kelp mooring tensions and grow line displacements. Conclusions are presented in Section 5.

## 2. Approximation of current velocity field using radial basis functions

Large-scale aquaculture installations often occupy substantial offshore sites where current velocities can vary considerably, depending on location and depth within the site, and changing with time. Therefore, the velocity data (usually provided in the form of scattered data points, as discussed in Section 3) must be approximated in space and time to make predictions on performance of the installations in spatially and temporally changing environmental conditions. By proper approximation, it is assumed such current velocity fields that are sufficiently smooth and accurate for meaningful numerical predictions.

The approximation method proposed in this paper is based on the concept of the radial basis function (RBF) interpolation (Majdisova and Skala, 2017) and has several advantages in approximating of current velocity fields. First, RBF interpolation is easily formulated, generalized and implemented for the input data of almost any dimension. Second, stability and good convergence properties of the method have been observed even in high-dimensional problems. Finally, RBF interpolation is a mesh-free method and is suitable for irregular spatial grid, meaning the points in the domain do not need to lie on a structured grid

(Wendland, 2005).

### 2.1. Radial basis function interpolation

With the RBF interpolation method, the current velocity field  $f(\mathbf{x})$  is obtained from  $n$  scattered data points such that  $f(\mathbf{x}_i) = f_i, i = 1, \dots, n$ , where  $\mathbf{x}$  is the  $d$ -dimensional coordinate of the arbitrary point,

$\mathbf{x}_i = (x_{i1}, x_{i2}, \dots, x_{id})$  is the coordinate of the scattered point  $i$ , and  $f_i$  is the value of current velocity at the point  $i$ . The number of dimensions  $d$  can include up to three spatial and one time variables, while the scalar function  $f$  is one of three current velocity projections on a spatial coordinate axes. The RBF interpolant,  $f(\mathbf{x})$ , is presented as a weighted sum of radial basis functions  $\varphi$  and often extended by a low-degree polynomial of vector of variables  $\mathbf{x}$  to improve fitting accuracy and extrapolation away from the data points (Holmström, 2008). Utilizing a linear polynomial, the representation of  $f(\mathbf{x})$  becomes:

$$f(\mathbf{x}) = \sum_{i=1}^n a_i \varphi(\|\mathbf{x} - \mathbf{x}_i\|_2) + \mathbf{b}^T \mathbf{x} + c \quad (1)$$

where  $\|\cdot\|_2$  is the Euclidian norm or the length of a vector. Weights  $a_1, a_2, \dots, a_n$ , vector of coefficients  $\mathbf{b} = (b_1, b_2, \dots, b_d)^T$  and the constant  $c$  are unknown, but can be found from the system of linear equations (SLE)

$$\begin{pmatrix} \varphi_{11} & \varphi_{21} & \cdots & \varphi_{n1} & x_{11} & x_{12} & \cdots & x_{1d} & 1 \\ \varphi_{12} & \varphi_{22} & \cdots & \varphi_{n2} & x_{21} & x_{22} & \cdots & x_{2d} & 1 \\ \vdots & \vdots & \ddots & \vdots & \vdots & \vdots & \ddots & \vdots & \vdots \\ \varphi_{1n} & \varphi_{2n} & \cdots & \varphi_{nn} & x_{n1} & x_{n2} & \cdots & x_{nd} & 1 \\ x_{11} & x_{21} & \cdots & x_{n1} & 0 & 0 & \cdots & 0 & 0 \\ x_{12} & x_{22} & \cdots & x_{n2} & 0 & 0 & \cdots & 0 & 0 \\ \vdots & \vdots & \ddots & \vdots & \vdots & \vdots & \ddots & \vdots & \vdots \\ x_{1d} & x_{2d} & \cdots & x_{nd} & 0 & 0 & \cdots & 0 & 0 \\ 1 & 1 & \cdots & 1 & 0 & 0 & \cdots & 0 & 0 \end{pmatrix} \begin{pmatrix} a_1 \\ a_2 \\ \vdots \\ a_n \\ b_1 \\ b_2 \\ \vdots \\ b_d \\ c \end{pmatrix} = \begin{pmatrix} f_1 \\ f_2 \\ \vdots \\ f_n \\ 0 \\ 0 \\ \vdots \\ 0 \\ 0 \end{pmatrix} \quad (2)$$

written in the symbolic matrix notations as

$$\Phi \mathbf{w} = \mathbf{F} \quad (3)$$

where  $\varphi_{lm} = \varphi_{ml} = \varphi(\|\mathbf{x}_l - \mathbf{x}_m\|_2)$ . Known conditions  $f(\mathbf{x}_i) = f_i, i = 1, \dots, n$ , represent the first  $n$  equations of the system, while last  $d+1$  equations are additional constraints on weights. Solving SLE (3) results in components of vector  $\mathbf{w} = \Phi^{-1} \mathbf{F}$  such that the interpolating function passes through all data points  $f_i$ . However, this RBF interpolation can lead to data overfitting. Fig. 1 shows an example of a typical overfitting of power-law-like function  $p(x) = 7x^{1/7}$  on regular data grids. This particular function was selected because it is often used by oceanographers to characterize average tidal velocity profiles (Lewis et al., 2017). The thin plate basis  $\varphi(r) = r^2 \log r$  was chosen in this case, but numerical experiments showed that changing basis to cubic, multiquadric and Gaussian forms do not resolve the overfitting issue, justifying the development of another approach.

Note that the approximation in this example is one-dimensional as it depends on variable  $x$  only. For multidimensional interpolations and approximations in this paper, regular grids were additionally rescaled to unit intervals between data points in each dimension to prevent gradient-related distortion of the resulting approximating function.

### 2.2. Radial basis functions approximation with Tikhonov regularization

The classic approach to address under- or overfitting and to control the interpolant capacity is to extend the hypothesis space by widening the class of functions representing the interpolant. This step was employed in Eq. (1) with the addition of a linear polynomial to the basic RBF interpolant. However, this approach is not universal since the nature of the data is not always known *a priori*.

Therefore, the under- and overfitting issues are addressed through regularization, another powerful tool to control the interpolant capacity.

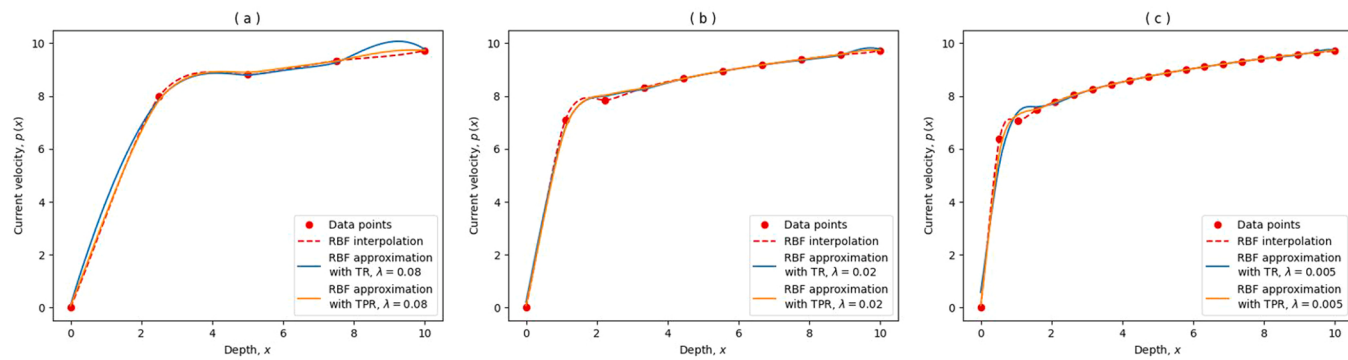


**Fig. 1.** Example of power law profile  $p(x) = 7x^{1/7}$  approximations on the ( a ) 5-point, ( b ) 10-point and ( c ) 20-point regular grids with thin plate basis.

In the process of regularization, problem (3) is reformulated in optimization terms. Instead of solving the SLE, it is now required to find such a vector of weights  $\mathbf{w}$  that minimizes the following cost function  $J$ :

$$J(\mathbf{w}) = \|\Phi\mathbf{w} - \mathbf{F}\|_2^2 \quad (4)$$

This is also known as the linear least squares problem. If  $\mathbf{w}$  makes cost function  $J(\mathbf{w})$  equal to zero, then it is the solution of the initial SLE described in Eq. (3). An objective of regularization is to modify the cost function to regulate properties of the resulting approximation. For example, one typical regularization technique, Tikhonov regularization (TR), changes cost function to

$$J(\mathbf{w}) = \|\Phi\mathbf{w} - \mathbf{F}\|_2^2 + \lambda \mathbf{w}^T \mathbf{w} \quad (5)$$

where positive parameter  $\lambda$  multiplied by regularizer  $\mathbf{w}^T \mathbf{w}$  provides a compromise between fitting the data and applying weights on fewer features. Although advanced techniques beyond the manual tuning of parameter  $\lambda$  exist (Hutter et al., 2015), our preliminary numerical experiments show that.

$\lambda = (d+1)/n^{2/d}$  provides a reasonable balance between smoothness and accuracy of the current velocity field, so it is utilized in the approximations applied in Section 4. The minimization problem (5) can be solved with matrix calculus, assuming that the cost function gradient is zero (Goodfellow et al., 2016):

$$\mathbf{w} = (\Phi^T \Phi + \lambda \mathbf{I})^{-1} \Phi^T \mathbf{F} \quad (6)$$

where  $\mathbf{I}$  is the identity matrix. It can be seen in Fig. 1b,c that the TR method somewhat smooths out the overfitting between second, third and fourth data points, however the regularization tends to distribute weights in a way that produces curve kinking, similar to the one between the last data points to the right in Fig. 1a,b and the first points to the left in Fig. 1c. The fitting issue occurs regardless of value of parameter  $\lambda$ , meaning that another regularization technique must be used.

### 2.3. Radial basis function approximation with thin plate regularization

Even though TR generally smooths the approximation functions, its performance is limited in regions of high convexity. Therefore, a regularization approach that utilizes the absolute values of second derivatives to restrict their growth is required. One of such approaches, known as thin plate regularization (TPR), refers to a physical analogy with energy due to bending of a thin plate. It was originally formulated for the function of two variables  $f(x, y)$  as follows:

$$\lambda \int_D \left[ \left( \frac{\partial^2 f}{\partial x^2} \right)^2 + 2 \left( \frac{\partial^2 f}{\partial x \partial y} \right)^2 + \left( \frac{\partial^2 f}{\partial y^2} \right)^2 \right] dx dy \quad (7)$$

where  $D$  is the domain of the function and the parameter  $\lambda$  is the so-called rigidity measure. The whole integral in (7) is also known as the

thin plate energy functional. The expression within the integral is the sum of all possible squared second derivatives, so it can be generalized for an arbitrary multivariate function  $f(\mathbf{x})$ :

$$\lambda \int_D [\mathbf{e}^T (\mathbf{H}_f \odot \mathbf{H}_f) \mathbf{e}] d\mathbf{x} \quad (8)$$

where  $\mathbf{H}_f$  is the Hessian matrix of  $f(\mathbf{x})$ ,  $\mathbf{e}$  is the vector of ones, and  $\odot$  is the Hadamard product (the element-wise matrix product). The product of Hessian matrices produces the symmetric matrix of the squared second derivatives and the multiplication by vectors of ones is used to obtain their sum.

If we now substitute function (1) into (8), a quadratic form of components  $\mathbf{w}$  is obtained. It is known that this quadratic form can be presented as the product

$$\lambda \mathbf{w}^T \mathbf{Q} \mathbf{w} \quad (9)$$

where  $\mathbf{Q}$  is the symmetric matrix of the quadratic form coefficients. The cost function  $J(\mathbf{w})$  corresponding to the thin plate regularization then becomes

$$J(\mathbf{w}) = \|\Phi\mathbf{w} - \mathbf{F}\|_2^2 + \lambda \mathbf{w}^T \mathbf{Q} \mathbf{w} \quad (10)$$

To minimize (10), the cost function gradient is assumed to be zero and solved for  $\mathbf{w}$  using matrix calculus:

$$\mathbf{w} = (\Phi^T \Phi + \lambda \mathbf{Q})^{-1} \Phi^T \mathbf{F} \quad (11)$$

Elements of the matrix  $\mathbf{Q}$  depend on the choice of RBF, which also influences behavior of the approximation. In practice, typical RBF choices have a cubic basis such that  $\phi(r) = r^3$  and with the thin plate basis of,  $\phi(r) = r^2 \log r$ . The thin plate basis was used since it minimizes the thin plate energy functional (8), however it does not mean that changing  $\lambda$  does not impact the resulting approximation.

### 2.4. Constrained optimization

Even though TPR resolves some of the TR fitting issues, the technique does not fit the boundary points well as shown on Fig. 1c. For this reason, the TPR approximations were constrained with additional equality conditions that require the values of approximating function at the boundary points to be equal to their values in the initial data set (Dirichlet boundary conditions). Thus, the TPR optimization problem

$$\min_{\mathbf{w}} J(\mathbf{w}), \quad J(\mathbf{w}) = \|\Phi\mathbf{w} - \mathbf{F}\|_2^2 + \lambda \mathbf{w}^T \mathbf{Q} \mathbf{w} \quad (12)$$

becomes

$$\min_{\mathbf{w} \in \mathcal{C}} J(\mathbf{w}), \quad \mathcal{C} = \{ \mathbf{w} \mid \|\Phi_c \mathbf{w} - \mathbf{F}_c\|_2^2 = 0 \} \quad (13)$$

where  $\Phi_c$  and  $\mathbf{F}_c$  are composed of the rows of  $\Phi$  and  $\mathbf{F}$ , respectively, that

correspond to the set of constrained points. To solve the constrained problem described in (13), it is reduced to an unconstrained optimization problem using the method of Lagrange multipliers. This approach introduces a new cost function called the generalized Lagrangian,

$$L(\mathbf{w}, \mu) = \|\Phi\mathbf{w} - \mathbf{F}\|_2^2 + \lambda\mathbf{w}^T\mathbf{Q}\mathbf{w} + \mu\|\Phi_c\mathbf{w} - \mathbf{F}_c\|_2^2 \quad (14)$$

solving the unconstrained optimization problem, equivalent to the one formulated in (13):

$$\min_{\mathbf{w}} \max_{\mu} L(\mathbf{w}, \mu) \quad (15)$$

where  $\mu$  is a scalar parameter. To resolve (15), the Lagrangian is minimized with respect to  $\mathbf{w}$  requiring  $\nabla_{\mathbf{w}}L(\mathbf{w}, \mu) = 0$ . The solution can be derived using matrix calculus as follows:

$$\mathbf{w}(\mu) = (\Phi^T\Phi + \lambda\mathbf{Q} + \mu\Phi_c^T\Phi_c)^{-1}(\Phi^T\mathbf{F} + \mu\Phi_c^T\mathbf{F}_c) \quad (16)$$

The maximization of  $\mu$  is obtained by equating the first derivative of the Lagrangian (14) with respect to  $\mu$  to zero:

$$\frac{\partial L}{\partial \mu} = \|\Phi_c\mathbf{w} - \mathbf{F}_c\|_2^2 = 0 \quad (17)$$

In this process, the value of parameter  $\mu$  is chosen such that the corresponding  $\mathbf{w}(\mu)$  in (16) satisfies (17). From the numerical standpoint, this could be resolved, for example, by performing a gradient ascent on  $\mu$ . To apply gradient ascent, step size  $\epsilon$ , precision  $\delta$  and initial value of  $\mu$  are first chosen. Then, the initial value of  $\mathbf{w}$  is calculated with (16). While  $\|\Phi_c\mathbf{w} - \mathbf{F}_c\|_2^2 > \delta$  is true, the parameter  $\mu$  changes to  $\mu + \epsilon(\partial L / \partial \mu)$ , and then new value of  $\mathbf{w}(\mu)$  is recalculated with (16). This iterative process for  $\mu$  and  $\mathbf{w}(\mu)$  continues until  $\|\Phi_c\mathbf{w} - \mathbf{F}_c\|_2^2 \leq \delta$ , when the final value of  $\mathbf{w}$  is obtained.

The choice of step size  $\epsilon$  influences the numerical performance of the gradient ascent since  $\mathbf{w}(\mu)$  in (16) must be recalculated at each iteration of  $\mu$ . Note that the set of boundary points for the irregular grid is found with the use of Delaunay triangulation and convex hull algorithms (<https://docs.scipy.org/doc/scipy/reference/spatial.html>).

Final comparison between the constrained RBF approximation with TPR, the RBF approximation with TR and the RBF interpolation of power-law-like function is shown in Fig. 1. The constrained RBF approximation with TPR completely resolves the fitting issue. The constrained approximation also provides good extrapolation for points outside of the domain. However, the values of the approximation function at these points are assumed to be equal to the grid point values at the nearest boundary.

### 3. Acquisition of the current velocity field data

The approach developed in Section 2 can be utilized to predict structural response of aquaculture installations to environmental loading regimes varying in space and time. Data sets describing the velocity distribution for a chosen marine site can be obtained through numerical prognostic models or by actual field measurements. Both of these approaches are discussed in this section, however, only the field measurements are used in Section 4.

#### 3.1. Numerical models

There are several known ocean dynamic models that can provide environmental data input for a chosen marine aquaculture site. For instance, the *Simulating WAves Nearshore* (SWAN) model, developed at Delft University of Technology, Netherlands, computes random, short-crested wind-generated waves in coastal regions and inland waters (Akpinar et al., 2012; Akpinar et al., 2016; Kutupoğlu et al., 2018; Liang et al., 2019). Another *Finite Volume Community Ocean Model* (FVCOM), developed by University of Massachusetts Dartmouth and Woods Hole Oceanographic Institution joint efforts, is originally focused on

flooding/drying process and the tidal-, buoyancy- and wind-driven circulation in the coastal region featured with complex irregular geometry and steep bottom topography (Chen et al., 2012). While other numerical models exist, FVCOM is of interest in the context of this paper since it is capable of producing discrete current velocity data sets.

FVCOM is an open-source code that consists of momentum, continuity, temperature, salinity and density equations and is closed physically and mathematically using turbulence closure submodels. This mathematical problem is then solved numerically by a discrete flux calculation in integral form of the governing equations over an unstructured triangular grid. This approach combines the advantages of finite-element methods (grid flexibility) and finite-difference methods (numerical efficiency and code simplicity), so the model is suitable for many coastal and interdisciplinary scientific applications (Chen et al., 2009, 2011; Qi et al., 2009). Numerical experiments have been performed to validate the non-hydrostatic FVCOM, including surface standing and solitary waves in idealized flat- and sloping-bottomed channels in homogeneous conditions, the density adjustment problem for lock exchange flow in a flat-bottomed channel, and two-layer internal solitary wave breaking on a sloping shelf (Lai et al., 2010). Benchmark test problems, such as Rossby equatorial soliton, the hydraulic jump, and the three-dimensional barotropic wind-driven basin, were performed to examine the properties of numerical dispersion and damping, the performance of the nonlinear advection scheme for supercritical flow conditions, and the accuracy of the implicit vertical viscosity scheme in barotropic settings, respectively (Huang et al., 2008).

Even though numerical models in general, and FVCOM in particular, are of use in marine science and ocean engineering, there are two limitations with respect to aquaculture operations. These models may not be applicable or available for all marine sites that are of interest for aquaculture installations, and if they are, the validation process takes years to achieve an acceptable level of accuracy; the numerical models are usually applied on large scales, so obtaining detailed current velocity distribution at locations that are only tens/hundreds of meters away from each other can be challenging. For these reasons, standard field current velocity measurements are still preferable for obtaining a reliable environmental data for a given aquaculture site.

#### 3.2. Field measurements. Current velocity acquisition at Wood Island site

*In-situ* current velocity measurements can be obtained with acoustic Doppler current profilers (ADCP), buoys monitored through special tracking devices and even satellites (Dohan and Maximenko, 2010), etc. The measurements deliver reliable and detailed current/wave information which makes them convenient data source for comprehensive current velocity field approximations. Thus, the multidimensional (in space and time) current velocity approximation technique presented in this paper was investigated and validated with a detailed ADCP current velocity data set obtained at the UNE Wood Island kelp farm research site, Maine, USA. The dataset was collected from May 16 to May 28, 2019. To obtain velocity components of tidal currents at Wood Island site, two ADCPs (west and east) were placed 42 m away from each other and 20–25 m away from the kelp grow line. The grow line and the ADCPs were deployed along the major axis of the tidal ellipse (Fig. 2). This orientation of the grow line ensured the best performance of claw anchors and minimized obstruction to navigation while wave and turbulence actions provided sufficient kelp nutrient concentration. The ADCPs used were 1 MHz acoustic wave and current sensors manufactured by Nortek (<https://www.nortekgroup.com/products/>).

Both ADCPs were installed 0.5 m up above the bottom, each in a tripod frame with a configuration that incorporates a 0.4 m blanking distance. The devices collected east-going, north-going and vertical components of current velocity at measurement points within the water column at 0.5 m depth bins starting from 0.9 m off the bottom to a maximum of 8.9 m above the acoustic transducers (Fig. 3). The

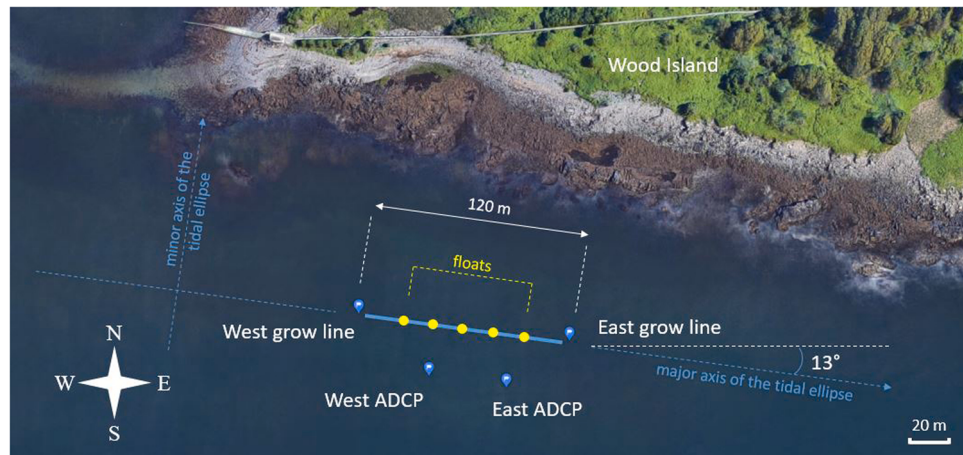


**Fig. 2.** Kelp farm deployment at University of New England Wood Island site, Maine, USA. West grow line: 43°27'17.54"N, 70°20'16.69"W; East grow line: 43°27'17.05"N, 70°20'11.45"W; West ADCP: 43°27'16.41"N, 70°20'14.94"W; East ADCP: 43°27'16.20"N, 70°20'13.01"W.

components were then projected on the major and minor axes of tidal ellipse, called major and minor axes hereafter, respectively, and averaged at 15 min time intervals (as 3 min averages from 0–3, 15–18, 30–33 and 45–48 min past each hour at 7 Hz sampling rate). Even though all three velocity components were measured, vertical component magnitudes were nearly zero during the whole monitoring time.

Fig. 4 shows three data samples of current profiles collected by the west and east ADCPs on May 16 (Fig. 4a), May 20 (Fig. 4b) and May 24, 2019 (Fig. 4c). The profiles were chosen for further numerical analysis and the velocity field approximations. These profiles were selected because they satisfy most of the following criteria: (1) absolute value of current velocity is high enough relative to other profiles; (2) west and east ADCP profile measurements were significantly different; (3) all other environmental measurements (water depth, wave height, wave

period and wave direction) are available for the same time interval. Projection of currents on the major axis dominates in the sample profiles, however the minor axis component can also be high near the neutral water line (Fig. 4c). Note that the profile measurements from the west and east ADCPs were taken at slightly different depths due to the difference in sea level elevations that included tides (Table 1), so the final value of mean velocity was obtained by averaging the west and east ADCP mean velocities.

In addition to the current velocity profiles, both east and west ADCPs were utilized in wave measuring mode to obtain pressures, velocities, and acoustic surface tracking (AST) characteristics. These parameters were acquired in bursts and processed to obtain time series, statistical, spectral, and directional wave information (Krogstad, 1988; Pedersen and Nylund, 2004; Siegel et al., 2006; Siegel, 2007; Pedersen and Siegel, 2008). The bursts were set to begin following each velocity profile measurement. Dynamic pressures and wave orbital velocities were sampled at 2 Hz for 1024 counts. AST data were measured at 4 Hz for 2048 counts, each for a duration of 8 min and 32 s to fit between velocity profile acquisitions (each for 512 s).

The wave datasets were then processed with the instrument software based on the Maximum Likelihood Method (Krogstad, 1988) modified for use with surface tracking (Pedersen and Nylund, 2004) to obtain wave spectral parameters such as the energy-based significant wave height and peak periods. The software also determined the average height of the top 1/3 waves from each surface-track time series.

Water depth variations, significant wave height (average height of top 1/3 waves), significant wave period and wave propagation direction were obtained and averaged over 15 min time intervals to synchronize them with the current velocity data, see Fig. 5. It can be seen that the significant wave height and significant wave period graphs for west and east ADCPs are almost identical (Fig. 5a,b), while the water depth varies due to a 0.7 m difference in sea floor level (Fig. 5d). The wave propagation direction demonstrated overall consistency being about 135° from true north except for the minor data noise between May 21 and May 24 (Fig. 5c). Mean velocity projections on major and minor axes are shown in Fig. 5e.

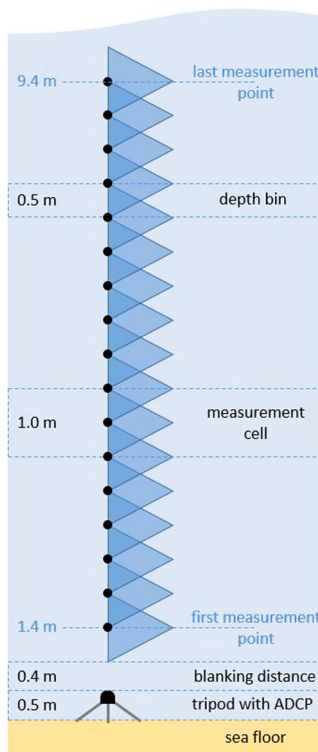


**Fig. 3.** Schematics of west/east ADCP deployed at UNE Wood Island site, Maine, USA.

#### 4. Numerical simulations of the Wood Island kelp farm

##### 4.1. Finite element model

The current velocity field approximation methodology presented in Section 2, was tested on the example of a kelp farm installed at the Wood Island research site in spring 2019. The 120 m long and 8 m high kelp farm was supported by two corner floats of 14.5 kg buoyancy with six

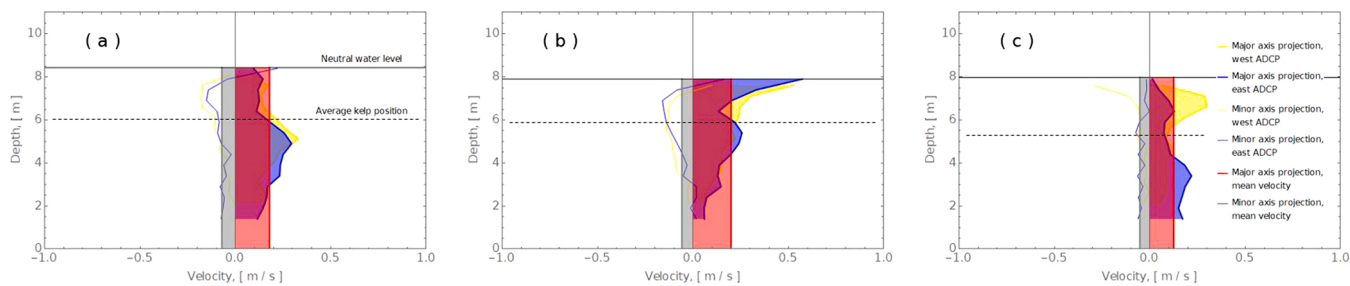


**Fig. 4.** Sample current profiles registered at (a) 16:00 on May 16, (b) 20:00 on May 20, (c) 23:15 on May 24, 2019, GMT-4.

**Table 1**

Environmental data samples registered at (a) 16:00 on May 16, (b) 20:00 on May 20, (c) 23:15 on May 24, 2019, GMT-4. Wave directions are degrees from true north.

Date sample		May 16	May 20	May 24
Significant wave height, [m]	West ADCP	0.23	0.32	0.22
	East ADCP	0.27	0.33	0.25
Significant wave period, [s]	West ADCP	11.40	6.10	6.41
	East ADCP	11.13	5.93	6.52
Wave direction, [°]	West ADCP	140.63	135.60	149.95
	East ADCP	122.36	136.39	132.67
Water depth, [m]	West ADCP	7.71	7.18	7.26
	East ADCP	8.44	7.90	7.98
Mean velocity, [m/s]	X-direction	0.18	0.20	0.13
	Y-direction	-0.07	-0.06	-0.05

intermediate floats of 4.5 kg buoyancy each (Fig. 6). The intermediate floats were equally distributed along the 60 m grow line in groups of two. Both grow and mooring lines were 1.2 cm in diameter nylon lines and were attached to 4.5 m long mooring chain at 20 kg that provided dampening to prevent snap of mooring lines and apply horizontal loading on the 30 kg steel claw anchors. Note that the buoys were attached to the grow line by nylon lines inside of polyvinyl (PVC) pipe to keep the kelp at a depth of 2 m. The grow line was oriented parallel to the major axis of the tidal ellipse for the best performance of the claw anchors.

To obtain properties of the kelp required for finite element analysis, the Wood Island kelp farm was inspected seven times from May 16 to May 28, 2019. During each of the inspections, the weight, volume, length (blade and stipe) and width (blades) of the kelp were measured at three points along the grow line. The measured data sets were averaged and produced 1.25 m long kelp that was assumed to be uniformly distributed along the grow line. The kelp was simulated using a technique similar to the “equivalent dropper approach” (Knysh et al., 2020) with the hydrodynamic characteristics (normal and tangential drag coefficients) taken from full-scale physical tests on dense aggregate of kelp blades (Fredriksson et al., 2020). The kelp elements were assigned the normal and tangential drag coefficients of 1.7 and 0.0577, respectively. For all other components of the farm, the coefficients were set at 1.2 and 0.01.

Finite element model of the kelp farm was built in *Hydro-FE* software developed from the well-validated *Aqua-FE* program developed at the University of New Hampshire (Gosz et al., 1996; Fredriksson et al., 2000; Tsukrov et al., 2000). The FORTRAN code of *Hydro-FE* uses the commercially available nonlinear finite element solver MSC.Marc with the MSC.Mentat (<https://www.mscsoftware.com/>) as graphical user interface. Multidimensional current profiles are implemented in *Hydro-FE* by constrained RBF approximation method described in Section 2. In the simulations presented in this paper, the values of significant wave height and period were used to obtain the corresponding JONSWAP wave spectrum with parameters of  $\alpha = 0.00035$ ,  $\gamma = 1$ ,  $\sigma = 0.07$  when  $\omega \leq \omega_p$ , and  $\sigma = 0.09$  when  $\omega > \omega_p$  (Rueda-Bayona et al., 2020). This spectrum was then reproduced in *Hydro-FE* by a finite

superposition of linear Airy waves characterized by their height, length and frequencies (Dean and Dalrymple, 1991).

The hydrodynamic forces exerted on the nodes are calculated with Morison equation (Morison et al., 1950; Goodman and Breslin, 1976). The contact between the seafloor and the mooring chains was simulated using techniques that has been previously implemented in *Hydro-FE* (Knysh et al., 2021). All components of the farm (grow line, mooring line, chain, etc.) were modeled with 2-node three-dimensional truss elements, except for the floats that were assumed to be beam elements. The number of elements used for each of the component, as well as the linear mass densities values are provided in Table 2.

Numerical simulations were performed with three sample current (Fig. 4), wave and depth (Table 1) data sets measured on May 16, May 20 and May 24, 2019. The 15 min simulation analysis time corresponded to 15 min field measuring intervals described in Section 3. The large strain case, the implicit dynamic single-step Houbolt transient operator and the lumped mass matrices were prescribed to Marc finite element solver in each simulation. The adaptive time steps were utilized and produced about 80,000 time increments in each simulation.

#### 4.2. Simulation results and discussion

Numerical predictions of the longline performance of the farm in this study were compared for four cases that represent different current field approximation strategies (Fig. 7). The first case, *mean velocity*, is the simplest approach (Fig. 7a). It is typically used when only one measuring device, such as an ADCP or a current meter, is available at the deployment site. The current is then assumed to be uniform with the magnitude equal either to the mean velocity through the depth (for the ADCP data) or to the current at the specific depth (for the current meter data). In this study, the mean velocity from the east ADCP location was used. The second case incorporated *linear interpolation* between the current profiles from the east ADCP (Fig. 7b). In the third case, *1D RBF approximation* is applied to the current profile obtained from the east ADCP data set (Fig. 7b). In this case, however, the constrained one-dimensional RBF current approximation approach from Section 2 was implemented. The fourth case, the *2D RBF approximation*, is based on both west and east ADCP data sets (Fig. 7c). The approximation in the fourth case was performed with the advanced constrained multidimensional RBF technique described in Section 2. Note that the average between wave data sets (wave direction, significant wave height and period) obtained by the west and east ADCPs was used in the *2D RBF approximation* case, while all other cases utilized the wave data set obtained by the east ADCP only.

Fig. 8 shows the kelp farm response comparison of the west mooring tension from the four cases. Almost identical west mooring line tensions are obtained for *linear interpolation* and *1D RBF approximation* cases in all three environmental loading scenarios (Fig. 8a,b,c) since they are based on the same data sets and must produce similar one-dimensional current profiles. It can be seen that the lowest difference in the predicted tensions is found from the low-magnitude profiles obtained on May 24, 2019 (Fig. 8c), where both major sources of drag, namely upper lines/

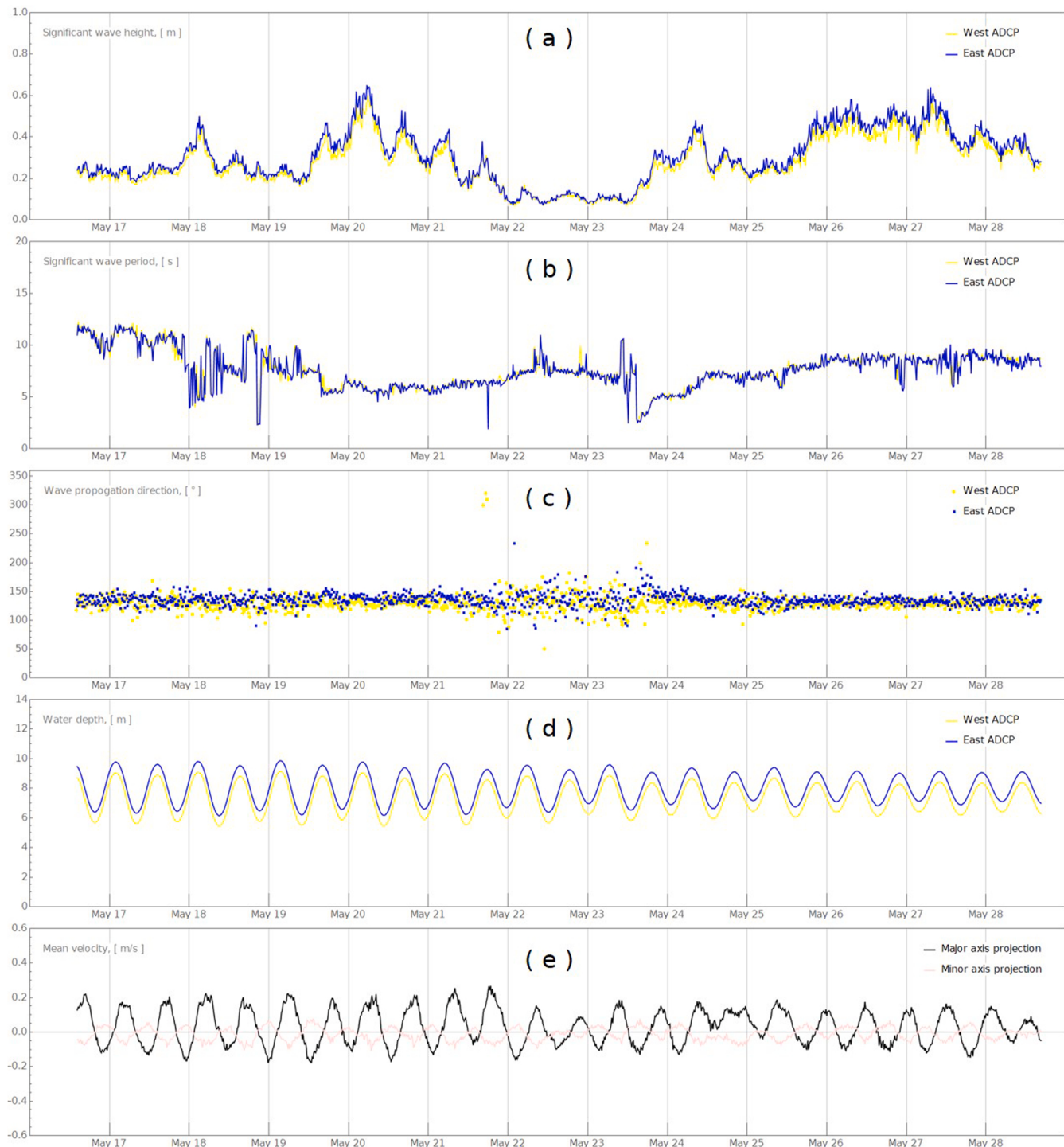


**Fig. 5.** Values of ( a ) significant wave height, ( b ) significant wave period, ( c ) wave direction, ( d ) water depth and ( e ) mean velocity registered by west and east ADCPs at UNE Wood Island site from May 16 to May 28, 2019. Wave propagation direction are degrees from true north. The west and east ADCP measurements are shown in yellow and blue, respectively.

floats and kelp, are subjected to the currents of about 0.10 m/s and lower (Fig. 4c).

Similar trends are also observed for the east mooring line tensions (Fig. 9), however values are noticeably lower than the west mooring tensions due to the east-dominated currents in all three sample data sets (Fig. 4). Fig. 9c demonstrates that lowest difference between the west and east tensions in all four current velocity approximation cases is naturally achieved for low-magnitude profile registered on May 24 (Fig. 4c).

More substantial differences in mooring line tensions are observed for high-magnitude velocity profiles observed on May 16 (Fig. 4a) and May 20 (Fig. 4b). For these datasets, the *mean velocity* case underpredicts both west and east mooring line tensions relative to other approximation techniques since magnitude of mean velocity is slightly lower than the magnitude of current velocity registered at the average kelp depth (Figs. 8a, 9a) and at the neutral water level (Figs. 8b, 9b). For example, the *mean velocity* profiles produce west mooring line tensions that are about 34–38 % lower than the tensions obtained in 2D RBF

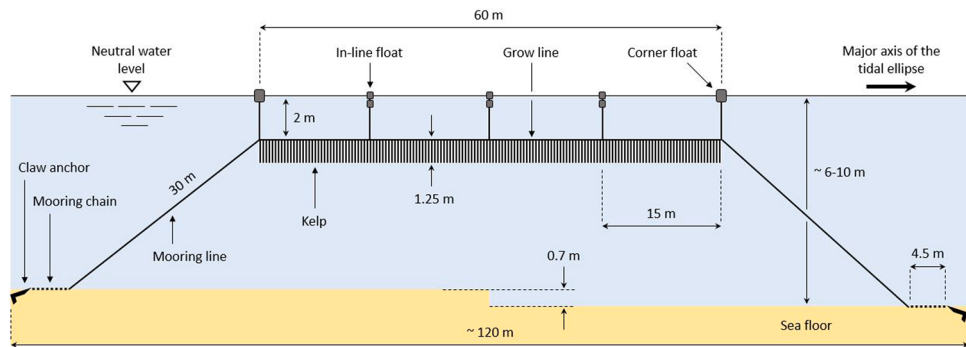


**Fig. 6.** Schematics of the Wood Island kelp farm. Not to scale.

**Table 2**

Linear density and number of finite elements assigned to the Wood Island kelp farm *Hydro-FE* model.

Kelp farm component	Linear mass density [kg/m]	Number of finite elements
Mooring/grow lines	0.13	266
Mooring Chains	4.45	16
Kelp (mass per grow line length)	11.27	1005
Buoys	–	8

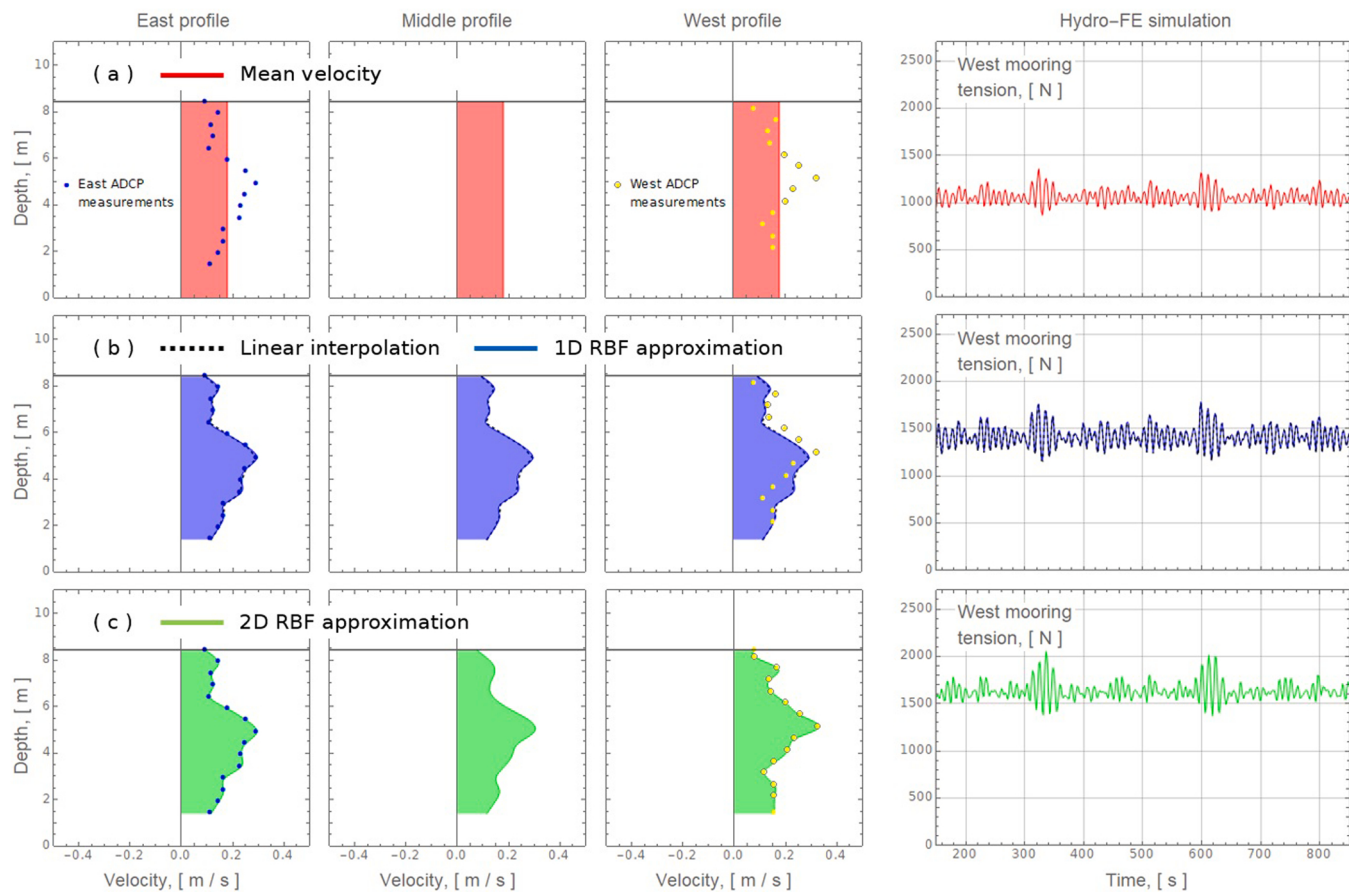


**Fig. 7.** Approximation of the current profile by ( a ) mean velocity, ( b ) linear interpolation and 1D RBF approximation, ( c ) 2D RBF approximation approaches used in *Hydro-FE* simulations. The predicted tensions of the west mooring are shown to the right. The East and West current velocity profiles are based on the ADCP measurements at the corresponding locations produced on May 16, 2019. The Middle profile is obtained using the considered approximations.

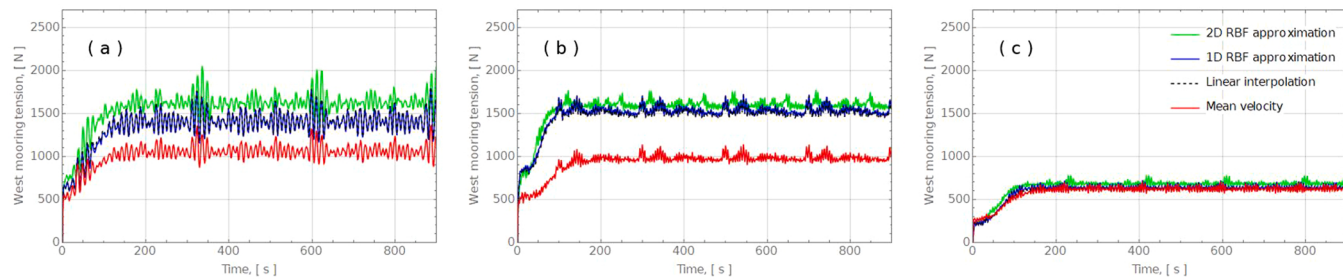


**Fig. 8.** West mooring line tensions obtained in *Hydro-FE* simulations using different current approximation techniques. The current and wave parameters are taken from data sets obtained at Wood Island site on ( a ) May 16, ( b ) May 20 and ( c ) May 24, 2019.

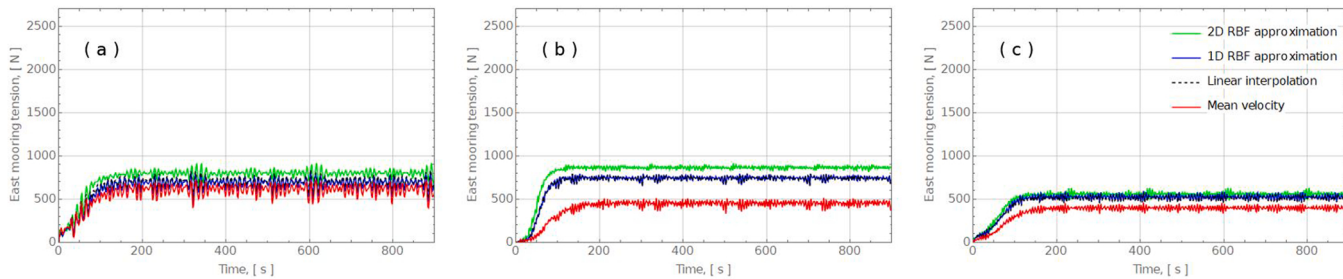


**Fig. 9.** East mooring line tensions obtained in *Hydro-FE* simulations using different current approximation techniques. The current and wave parameters are taken from data sets obtained at Wood Island site on ( a ) May 16, ( b ) May 20 and ( c ) May 24, 2019.

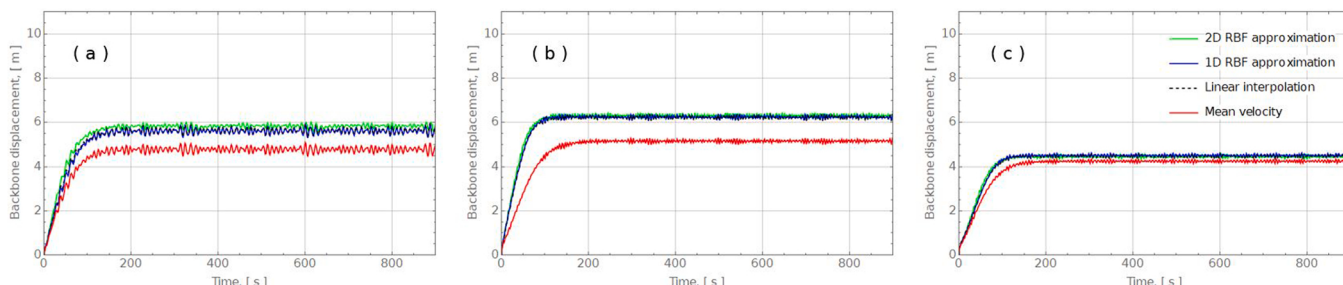


**Fig. 10.** Displacement of the grow line middle obtained in *Hydro-FE* simulations using different current approximation techniques. The current and wave parameters are taken from data sets obtained at Wood Island site on ( a ) May 16, ( b ) May 20 and ( c ) May 24, 2019.

approximation cases. (Fig. 8a,b). This discrepancy range is even higher for east mooring line tensions, being about 22–47 % (Fig. 9a,b).

The difference between *2D RBF approximation* and *1D RBF approximation* cases are of special interest when selecting the most robust approximation technique. It was found that even a small divergence of about 0.03 m/s in west and east ADCP current measurements at the average kelp depth (in the major axis direction) can lead to 15 % increase in the predicted highest (west, to be exact) mooring line tension (Fig. 8a). Even with the close distance of 42 m between west and east ADCPs at Wood Island site, comparing to the scale of typical large aquaculture installations, utilization of a more accurate *2D RBF approximation* makes substantial difference in evaluating the kelp farm performance. Note that for current measurements on May 20, 2019 (Fig. 4b), the increase in mooring tension is only 7 % that is attributed to magnitude of current velocity measured by the west ADCP being higher than the magnitude of the current velocity measured by the west ADCP at the depths between average kelp position and neutral water level (Fig. 4b).

The total grow line displacement of the Wood Island kelp farm for the four current velocity approximation techniques were also compared in terms of a displacement of the grow line's middle point. Fig. 10 shows the overall displacement (including three components) of the grow line middle for the data sets registered on May 16 (Fig. 10a), May 20

(Fig. 10b) and May 24, 2019 (Fig. 10c). It was found that the difference in the displacements between *linear interpolation*, *1D RBF approximation* and *2D RBF approximation* cases is practically negligible being less than 2 %. It was also found that the *mean velocity* profile predicts displacements that are substantially lower, similar to what was observed for mooring line tensions. The difference in displacements reaches up to 6–18 % depending on the environmental data sets considered.

## 5. Conclusions

Distribution of currents at large-scale offshore aquaculture sites is usually available as a set of discrete data points obtained from measurements or ocean dynamic models. This paper proposes an efficient methodology to approximate the discrete multidimensional current velocity data for numerical analysis as applied to ocean deployed aquaculture installations. The current velocities at such marine sites can spatially vary, so applying accurate and smooth current field approximations are essential to estimate the performance of the aquaculture system.

The meshless radial basis function approximation method produces such smooth and accurate approximation of discrete current velocity data obtained from field measurements and works on both regular and irregular grids. However evenly distributed data points in each

dimension are still recommended. Numerical experiments showed that possible under- or overfitting of the radial basis function approximation are addressed with a combination of domain rescaling, thin plate regularization and constraining the approximation values at boundary points.

The proposed current approximation method was implemented in *Hydro-FE* software and tested on the example of kelp farm deployed at Wood Island research site in Maine, USA. Numerical simulations of the farm were performed using field velocity measurements conducted in spring 2019.

It is shown that the difference in the mooring line tensions of the kelp farm can reach up to 34–38 % between mean velocity profile and two-dimensional radial basis function approximation, or 15 % between one- and two-dimensional radial basis function approximations. The total displacements of the grow line middle turned out to be practically the same for all approximation techniques, except for mean velocity, where the displacements appear to be 6–18 % lower. This means that additional measurements combined with the advanced approximation method presented in this paper allows to substantially improve prediction of aquaculture installation performance.

## Declaration of Competing Interest

The authors declare that they have no known competing financial interests or personal relationships that could have appeared to influence the work reported in this paper.

## Acknowledgements

The authors thank the US Department of Energy's ARPA-E, US program for funding the project (award no. DE-AR0000923). We also appreciate help and expertise of Callentis Consulting Group in the multidimensional approximation methods. Support was also obtained from the ARPA-E interagency agreement with the United States Naval Academy 89703018SAR000002 and project award number DE-AR0000917 with the University of New England, US.

## References

- Akpınar, A., van Vledder, G.P., Kömürcü, M.I., Özger, M., 2012. Evaluation of the numerical wave model (SWAN) for wave simulation in the Black Sea. *Cont. Shelf Res.* 50–51, 80–99. <https://doi.org/10.1016/j.csr.2012.09.012>.
- Akpınar, A., Bingölbali, B., Van Vledder, G.P., 2016. Wind and wave characteristics in the Black Sea based on the SWAN wave model forced with the CFSR winds. *Ocean Eng.* 126, 276–298. <https://doi.org/10.1016/j.oceaneng.2016.09.026>.
- Asche, F., Cojocaru, A.L., Roth, B., 2018. The development of large scale aquaculture production: a comparison of the supply chains for chicken and salmon. *Aquaculture* 493, 446–455. <https://doi.org/10.1016/j.aquaculture.2016.10.031>.
- Bi, C.W., Chen, Q.P., Zhao, Y.P., Su, H., Wang, X.Y., 2020. Experimental investigation on the hydrodynamic performance of plane nets fouled by hydroids in waves. *Ocean Eng.* 213, 107839. <https://doi.org/10.1016/j.oceaneng.2020.107839>.
- Chen, C., Beardsley, R.C., Cowles, G., Qi, J., Lai, Z., Gao, G., Stuebe, D., Xu, Q., Xue, P., Ge, J., Ji, R., Hu, S., Tian, R., Huang, H., Wu, L., Lin, H., 2012. An Unstructured-Grid, Finite-Volume Community Ocean Model: FVCOM user manual. Sea Grant College Program. Massachusetts Institute of Technology.
- Chen, C., Gao, G., Qi, J., Proshutinsky, A., Beardsley, R.C., Kowalik, Z., Lin, H., Cowles, G., 2009. A new high-resolution unstructured grid finite volume Arctic Ocean model (AO-FVCOM): An application for tidal studies. *J. Geophys. Res.* 114, 1–20. <https://doi.org/10.1029/2008jc004941>.
- Chen, C., Huang, H., Beardsley, R.C., Xu, Q., Limeburner, R., Cowles, G.W., Sun, Y., Qi, J., Lin, H., 2011. Tidal dynamics in the Gulf of Maine and New England Shelf: an application of FVCOM. *J. Geophys. Res. Ocean.* 116, 1–14. <https://doi.org/10.1029/2011JC007054>.
- Dean, R.G., Dalrymple, R.A., 1991. Water wave mechanics for engineers and scientists, Engineering.
- Dohan, K., Maximenko, N., 2010. Monitoring ocean currents with satellite sensors. *Oceanography* 23, 94–103. <https://doi.org/10.1088/0305-4624/18/6/301>.
- Fairbanks, L., 2016. Moving mussels offshore? Perceptions of offshore aquaculture policy and expansion in New England. *Ocean Coast. Manag.* 130, 1–12. <https://doi.org/10.1016/j.ocecoaman.2016.05.004>.
- Fredriksson, D.W., DeCew, J.C., Tsukrov, I., Swift, M.R., Irish, J.D., 2007. Development of large fish farm numerical modeling techniques with in situ mooring tension comparisons. *Aquac. Eng.* 36, 137–148. <https://doi.org/10.1016/j.aquaeng.2006.10.001>.
- Fredriksson, D.W., Dewhurst, T., Drach, A., Beaver St., W., Gelais, A.T., Johndrow, K., Costa-Pierce, B.A., 2020. Hydrodynamic characteristics of a full-scale kelp model for aquaculture applications. *Aquac. Eng.* 90, 102086. <https://doi.org/10.1016/j.aquaeng.2020.102086>.
- Fredriksson, D.W., Swift, M.R., Muller, E., Baldwin, K., Celikkol, B., 2000. Open ocean aquaculture engineering: system design and physical modeling. *Mar. Technol. Soc. J.* <https://doi.org/10.4031/MTSJ.34.1.5>.
- Gentry, R.R., Lester, S.E., Kappel, C.V., White, C., Bell, T.W., Stevens, J., Gaines, S.D., 2017. Offshore aquaculture: Spatial planning principles for sustainable development. *Ecol. Evol.* 7, 733–743. <https://doi.org/10.1002/ece3.2637>.
- Goodfellow, I., Bengio, Y., Courville, A., 2016. Deep Learning. MIT Press.
- Goodman, T., Breslin, J., 1976. Statics and dynamics of anchoring cables in waves. *J. Hydraulics* 10, 113–120.
- Gosz, M., Kestler, K., Swift, M.R., Celikkol, B., 1996. Finite Element Modeling of Submerged Aquaculture Net-Pen Systems. *Open Ocean Aquac. Proc. Int. Conf. 8–10. Holmström, K., 2008. An adaptive radial basis algorithm (ARBF) for expensive black-box global optimization. *J. Glob. Optim.* 41, 447–464. <https://doi.org/10.1007/s10898-007-9256-8>.*
- Huang, H., Chen, C., Cowles, G.W., Winant, C.D., Beardsley, R.C., Hedstrom, K.S., Haidvogel, D.B., 2008. FVCOM validation experiments: comparisons with ROMS for three idealized barotropic test problems. *J. Geophys. Res. Ocean.* 113, 1–14. <https://doi.org/10.1029/2007JC004557>.
- Hutter, F., Lücke, J., Schmidt-Thieme, L., 2015. Beyond manual tuning of hyperparameters. *KI - Kunstl. Intell.* 29, 329–337. <https://doi.org/10.1007/s13218-015-0381-0>.
- Klebert, P., Patrusson, Ø., Endresen, P.C., Rundtop, P., Birkevold, J., Rasmussen, H.W., 2015. Three-dimensional deformation of a large circular flexible sea cage in high currents: field experiment and modeling. *Ocean Eng.* 104, 511–520. <https://doi.org/10.1016/j.oceaneng.2015.04.045>.
- Knysh, A., Coyle, J., Decew, J., Drach, A., Swift, M.R., Tsukrov, I., 2021. Floating protective barriers: evaluation of seaworthiness through physical testing, numerical simulations and field deployment. *Ocean Eng.*, 108707. <https://doi.org/10.1016/j.oceaneng.2021.108707>.
- Knysh, A., Tsukrov, I., Chambers, M., Swift, M.R., Sullivan, C., Drach, A., 2020. Numerical modeling of submerged mussel longlines with protective sleeves. *Aquac. Eng.* <https://doi.org/10.1016/j.aquaeng.2019.102027>.
- Krogstad, H.E., 1988. Maximum likelihood estimation of ocean wave spectra from general arrays of wave gauges. *Model. Identif. Control.* <https://doi.org/10.4173/mic.1988.2.3>.
- Kutupoğlu, V., Çakmak, R.E., Akpinar, A., van Vledder, G.P., 2018. Setup and evaluation of a SWAN wind wave model for the Sea of Marmara. *Ocean Eng.* 165, 450–464. <https://doi.org/10.1016/j.oceaneng.2018.07.053>.
- Lai, Z., Chen, C., Cowles, G.W., Beardsley, R.C., 2010. A nonhydrostatic version of FVCOM 1. Valid. *Exp. J. Geophys. Res. Ocean* 115, 1–23. <https://doi.org/10.1029/2009JC005525>.
- Lewis, M., Neill, S.P., Robins, P., Hashemi, M.R., Ward, S., 2017. Characteristics of the velocity profile at tidal-stream energy sites. *Renew. Energy* 114, 258–272. <https://doi.org/10.1016/j.renene.2017.03.096>.
- Liang, B., Gao, H., Shao, Z., 2019. Characteristics of global waves based on the third-generation wave model SWAN. *Mar. Struct.* 64, 35–53. <https://doi.org/10.1016/j.marstruc.2018.10.011>.
- Majdisova, Z., Skala, V., 2017. Radial basis function approximations: comparison and applications. *Appl. Math. Model.* 51, 728–743. <https://doi.org/10.1016/j.apm.2017.07.033>.
- Morison, J.R., Johnson, J.W., Schaaf, S.A., 1950. The force exerted by surface waves on piles. *J. Pet. Technol.* 2, 149–154. <https://doi.org/10.2118/950149-G>.
- Nguyen, T.X., Winger, P.D., 2016. Numerical modeling - a comparison of different methods for simulating Bottom Trawls. *Fish. Technol.* 53, 9–29.
- Pedersen, T., Nylund, S., 2004. Wave height measurements using acoustic surface tracking. *USA Balt. Int. Symp.* 1234–1241. <https://doi.org/10.1109/BALTIC.2004.7296806>.
- Pedersen, T., Siegel, E., 2008. Wave measurements from a subsurface buoy. *Sea Tech.* 42, 17–20.
- Pribadi, A.B.K., Donatini, L., Lataire, E., 2019. Numerical modelling of a mussel line system by means of lumped-mass approach. *J. Mar. Sci. Eng.* 7. <https://doi.org/10.3390/jmse7090309>.
- Qi, J., Chen, C., Beardsley, R.C., Perrie, W., Cowles, G.W., Lai, Z., 2009. An unstructured-grid finite-volume surface wave model (FVCOM-SWAVE): Implementation,

- validations and applications. *Ocean Model* 28, 153–166. <https://doi.org/10.1016/j.ocemod.2009.01.007>.
- Rueda-Bayona, J.G., Guzmán, A., Silva, R., 2020. Genetic algorithms to determine JONSWAP spectra parameters. *Ocean Dyn.* 70, 561–571. <https://doi.org/10.1007/s10236-019-01341-8>.
- Siegel, E., 2007. New methods for subsurface wave measurements at offshore locations. *Oceans New Tech* 13, 2–3.
- Siegel, E., Pedersen, T., Maatje, J., 2006. Real-time directional wave measurements. *Sea Tech* 47, 10–14.
- Smith, T.M., Livezey, R.E., Shen, S.S., 1998. An improved method for analyzing sparse and irregularly distributed SST data on a regular grid: the Tropical Pacific Ocean. *J. Clim.* 11, 1717–1729. [https://doi.org/10.1175/1520-0442\(1998\)011<1717:aimfas>2.0.co;2](https://doi.org/10.1175/1520-0442(1998)011<1717:aimfas>2.0.co;2).
- Thierry, N.N.B., Tang, H., Xu, L., Hu, F., 2019. Effect of mesh size, twine material and trawl gear accessories on the bottom trawls hydrodynamic performance. *Int. J. Fish. Aquat. Res.* 4, 01–09.
- Tsukrov, I.I., Ozbay, M., Swift, M.R., Celikkol, B., Fredriksson, D.W., Baldwin, K., 2000. Open ocean aquaculture engineering: numerical modeling. *Mar. Technol. Soc. J.* 34, 29–40. <https://doi.org/10.4031/MTSJ.34.1.4>.
- Wendland, H., 2005. *Scattered Data Approximation*. World Scientific.
- Wintherøig-Rasmussen, H., Simonsen, K., Patursson, Ø., 2016. Flow through fish farming sea cages: comparing computational fluid dynamics simulations with scaled and full-scale experimental data. *Ocean Eng.* 124, 21–31. <https://doi.org/10.1016/j.oceaneng.2016.07.027>.
- Zhao, Y.P., Wang, X.X., Decew, J., Tsukrov, I., Bai, X.D., Bi, C.W., 2015. Comparative study of two approaches to model the offshore fish cages. *China Ocean Eng.* 29, 459–472. <https://doi.org/10.1007/s13344-015-0032-0>.